Exploring the dynamical transitions on an epileptic hippocampal network model and its modulation strategy based on transcranial magneto-acoustical stimulation

Liyuan Zhang[a], Yuejuan Xu[a], Gerold Baier[b], Youjun Liu[a], Bao Li[a,*]

[a] Department of Biomedical Engineering, College of Chemistry and Life Science, Beijing University of Technology, Beijing, 100124, China

[b] Cell and Developmental Biology, University College London, London, WC1E 6BT, UK

[*]Corresponding author: Bao Li (libao@bjut.edu.cn)

Abstract: The mechanisms of network and transition dynamics of epileptiform activity remain unclear. In general, the transitions of epileptiform discharges comprise slow interictal discharges, ictal discharges and postictal depression. Studies have indicated that network properties and the inherent parameters of neuronal models have great impacts on the transitions. Recently, a novel neuromodulation technique, transcranial magneto-acoustical stimulation (TMAS), has been tested for its efficiency experimentally and computationally. In this paper, we establish a biophysical computational network model of an ictogenic hippocampus area to investigate the underlying transitions mechanisms and reveal neuromodulation mechanisms combined with TMAS. Results demonstrate that long distance connections caused by increased connection probability and the number of nearest-neighbour edges make the network more random and focused. The cooperation of network topological structure and neuronal parameters including ion concentration and inherent external input of neurons could induce epileptic transitions. Moreover, the focused ultrasound transducer has the ability to launch and focus the transcranial ultrasound wave to the hippocampal area in the depth of the three-layer tissue. By coupling with a static magnetic field, the proposed modulated induced TMAS currents can terminate epileptiform activity but consumes more energy by regulating magnetic strength. However, changing modulation frequency was unable to fully suppress seizures. These computational results offer an explanation of the mechanisms of neurodynamics of epileptiform discharges and its neuromodulation by TMAS.

Keywords: Hippocampal network, dynamical transitions, epileptiform activity, transcranial magneto-acoustical stimulation (TMAS)

1. Introduction

Epilepsy is a chronic non-communicable disease of the brain that affects about 50 million people worldwide, which makes it one of the most important neurological diseases globally [1]. Temporal lobe epilepsy (TLE) is the most frequent type of drug-resistant epilepsy. TLE is also defined as a category of focal epilepsy which is associated with hippocampal sclerosis [2]. Research using magnetic resonance imaging (MRI) and functional MRI demonstrated that TLE is a network disorder [3], which enables us to employ theories of network topology and network dynamics to quantify properties for such a complex system. Evidence from MRI illustrated in TLE patients that brain networks have the characteristics of a small-world [4], which is originally proposed by Watts and Strogatz in 1998 [5], and simulations of seizure-like activity based on hippocampal slice electrophysiology also illustrated small-world property [6][7]. Most biological and social networks are highly clustered as regular graph and have small characteristic paths as predicted by random networks. Compared to random networks, systems with the small-world structure have more efficient signal-propagation velocity and synchronization. In terms of an ictogenic zone in the hippocampus area, the excitatory pyramidal cells and the inhibitory interneurons communicate with each other mainly mediated by α-amino-3-hydroxy-5-methyl-4-isoxazole-propionicacid (AMPA) and γ-aminobutyric acid type A ($GABA_A$) receptors [8]. Some observations that epileptiform activities could be induced by increasing the extracellular concentration of potassium ions [9]. Other research also demonstrated that the inherent external input of neurons can interfere with epileptic seizure activity [10][11]. However, the neural circuits of hippocampus are complex, and the mechanisms of seizure activity are not well revealed. Some hippocampal computational models have been proposed to describe the dynamics of epilepsy, for example, cellular network models [12-14]. These cellular network models allow to analyse the characteristics of the discharge patterns both as a function of ion concentration and network topology. Another widely used approach is the Neural Mass Model (NMM), which is a mesoscopic model considering the average activity of interneuron and principal neuron populations [15]. It was used to describe epileptogenesis caused by the glutamatergic and GABAergic

dynamics in a hippocampal region [16]. By adopting these modeling methodologies, we established a computational biophysical network of the hippocampus with small-world connectivity structure to explore the network dynamics of epileptiform transitions.

Neuromodulation techniques have been explored for the treatment of drug-resistant epilepsy and other neurological diseases [17], examples being invasive vagus nerve stimulation (VNS) [18], and deep brain stimulation (DBS) [19]. Optogenetic stimulation has also been used for the intervention in spontaneous hippocampal seizures [20]. Besides this, some non-invasive methods, e.g., transcranial magnetic stimulation (TMS), transcranial direct current stimulation (tDCS), and ultrasound technologies have been shown to be efficient in suppressing seizures [21-23]. Computational studies also investigated the stimulation mechanisms underlying a potential therapy for epilepsy [24][25]. Transcranial magneto-acoustical stimulation (TMAS) is a novel brain neuromodulation that is noninvasivene, deep brain focused, and has a high spatial resolution [26]. TMAS combines the advantages of magnetic and focused ultrasound and employs the current induced by a static magnetic field and transcranial focused ultrasound to activitate or suppress neurons [27]. The formation of TMAS was proposed by Norton [26] in 2003. Yuan et al. investigated the influence of TMAS on the spiking rhythms of Hodgkin-Huxley neuronal model from a computational view [28]. Zhou et al. built a Parkinson's disease (PD) experimental mouse model to test the effects of high-resolution transcranial electrical stimulation based on magneto-acoustics and then explored the potential mechanism of TMAS [29]. In 2021, Zhang et al. designed a regular distribution array ultrasound transducer of an opening diameter 112mm with a radius of curvature of 86mm to realize focused ultrasound in a (computational) three-layer brain area. Numerical simulation results including the influences of input intensity, repetition frequencies and duty cycle of TMAS were discussed for the treatment of PD [27]. Previous studies have shown that both static magnetic field [30] and noninvasive ultrasonic neuromodulation [31] can effectively suppressing seizures, which provided experimental basis for TMAS in the treatment of epilepsy. However, the therapeutic effects of TMAS on epilepsy need further

research in both theoretically and experimentally. Motivated by these pioneering studies, we establish a TMAS computational model consisting of a bowel shaped focused ultrasound transducer, a static magnet and a three-layer brain area from anatomy data. We show that the simulated TMAS model has the ability of focusing the neuromodulation effect on the deep hippocampus area. Moreover, induced TMAS current is added to the biophysical network to explore the influence of modulating signals, the magnetic field intensity, and the modulation frequency on epileptiform activities. Finally, dynamical transition mechanisms underlying different TMAS strategies are investigated.

2. Methods and materials

2.1. Configuration of hippocampal neural network

The hippocampal pyramidal cell model of Olufsen and colleagues [32] is used as a hippocampus network model. Two ionic currents are used: a fast sodium current and potassium hyperpolarization. For the soma compartment of a pyramidal cell, the membrane potential and ionic current can be computed by the equations:

$$\begin{cases} C_m\dot{V} = g_{Na}m_\infty(V)^3h(V_{\mathrm{Na}} - V) + g_K n^4(V_K - V) + g_L(V_L - V) + I_e \\ \dot{h} = \frac{h_\infty(V)-h}{\tau_h(V)} \\ \dot{n} = \frac{n_\infty(V)-h}{\tau_n(V)} \end{cases} \quad (1)$$

The corresponding parameter values for a pyramidal cell are $C_m = 1\mu\mathrm{F/cm}^2$, $g_{Na} = 100\mathrm{mS/cm}^2$, $g_K = 80\mathrm{mS/cm}^2$, $g_L = 0.1\mathrm{mS/cm}^2$, $V_{Na} = 50\mathrm{mV}$ and $V_L = -67\mathrm{mV}$. These state variables follow the Hodgkin-Huxley type equations [33] in Eq. (1) is this paper where $x_\infty(V) = \alpha_x(V)/\big(\alpha_x(V) + \beta_x(V)\big)$for $x = m, h$ or n, $\tau_x(V) = 1/\big(\alpha_x(V) + \beta_x(V)\big)$ for $x =$ h or n. The rate functions are presented in Table 1. Here the potassium ion potential $V_{K_{ex}}$ and the external current input for the excitatory cell I_e are crucial

parameters which respond to the inherent neuronal characteristics of the network. We consider their ranges from -50mV to -100 mV and 0.2 μA/cm^2 to 1 μA/cm^2, respectively.

A single compartmental model is used for the inhibitory interneuron [34], which follows the current equations as in the pyramidal cell. The respective parameter values are $C_m = 1\mu\text{F/cm}^2$, $g_{Na} = 35\text{mS/cm}^2$, $g_K = 9\text{mS/cm}^2$, $g_L = 0.1\text{mS/cm}^2$, $V_{Na} = 55\text{mV}$, $V_K = -90\text{mV}$ and $V_L = -65\text{mV}$. The external driven current for the inhibitory cell $I_i = 0.3\mu\text{A/cm}^2$. In the equations of state variables, $\tau_x(V)$ is replaced by $\tau_x(V) = 0.2/\big(\alpha_x(V) + \beta_x(V)\big)$ for the interneuron model, other rate functions are specified in Table 1.

For synaptic connections between cells, the synaptic gating variable s obeys the principle $\dot{s} = \rho(V)(1-s)/\tau_R - s/\tau_D$ [35]. Here $\rho(V) = \big(1 + \tanh(V/4)\big)/2$ is a Heaviside function. Furthermore, the synaptic current can be expressed as $I_{\text{syn}_{ij}} = g_{ij}s_i(t)\big(V_{\text{rev}} - V_j\big)$ which indicates the synaptic current from cell i to cell j. An AMPA-type synapse connects pyramidal to pyramidal cells and pyramidal cells to interneurons. The parameters for AMPA synapses from pyramidal to pyramidal cell are $g_{PC\to IN} = 0.001\text{mS/cm}^2$, $g_{PC\to PC} = 0.0001\text{mS/cm}^2$, $\tau_R = 0.1$, $\tau_D = 3$, and $V_{rev} = 0\text{mV}$. The GABA_A synapses originating from interneurons target both pyramidal cells and interneurons. The values of the parameters are $g_{IN\to PC} = 0.001\text{mS/cm}^2$, $g_{IN\to IN} = 0.03\text{mS/cm}^2$, $\tau_R = 0.3$, $\tau_D = 9$ and $V_{rev} = -80\text{mV}$.

Studies have shown evidence that epilepsy is a network-level disorder and exhibits characteristics of small-world network topology [36]. In addition, Netoff et al. introduced a hippocampal slice model (CA1 and CA3 regions) with small-network structure [6]. They reproduced normal, seizing and bursting behaviors by changing the synaptic strengths and other parameters. They employed this network model to explain specific changes in topology or synaptic strength induce transitions from normal to epileptic bursting. Therefore, we use the small-world network topology to construct a hippocampal neuronal network. From Watts and Strogatz's study, the rule of the rewiring procedure can be described as: start

from a ring lattice with N nodes and K edges per node, rewire each edge at random with probability $p(0 < p < 1)$. When $p = 0$ the network shows the property of characteristic path length $L(p)$ growing linearly with N, i.e., a highly clustered regular network, and $L(p)$ grows logarithmically with N and demonstrates less clustered (random network) if $p = 1$ [5]. In general, the structural properties of the above graphs can be quantified by $L(p)$ and clustering coefficient $C(p)$. The quantitative description is: $L(p) \sim \frac{N}{2k} \gg 1$ and $C(p) \sim \frac{3}{4}$ as p goes to 0, while $L(p) \sim \frac{\ln(n)}{\ln(k)}$ and $C(p) \sim \frac{k}{n}$ when p goes to 1[5]. The detail theory can be found in Ref.[5]. The configuration of our small-world networks is characterized by the network size $N = 1000$ (800 pyramidal cells and 200 interneurons, we consider this size as an example), K edges per node, i.e., the number of synaptic connections per neuron, and the connection probability p. We scan K from 50 to 450 and p from 0.1 to 0.9, respectively. By combing the inherent neuronal characteristics with the network configuration properties, we are able to induce normal and epileptiform behaviors.

TABLE 1 Rate functions for pyramidal cell and interneuron [33][34]

Neuron type	Forward rate function	Backward rate function
Pyramidal cell	$\alpha_m(V) = \frac{0.32(V+54)}{1-\exp(-(V+54)/4)}$	$\beta_m(V) = \frac{0.28(V+27)}{\exp((V+27)/5)-1}$
	$\alpha_h(V) = 0.128\exp(-(V+50)/18)$	$\beta_h(V) = \frac{4}{1+\exp(-(V+27)/5)}$
	$\alpha_n(V) = \frac{0.032(V+52)}{1-\exp(-(V+52)/5)}$	$\beta_n(V) = 0.5\exp(-(V+57)/40)$
Interneuron	$\alpha_m(V) = \frac{0.1(V+35)}{1-\exp(-(V+35)/10)}$	$\beta_m(V) = 4\exp(-(V+60)/18)$
	$\alpha_h(V) = 0.07\exp(-(V+58)/20)$	$\beta_h(V) = \frac{1}{\exp(-0.1(V+28))+1}$
	$\alpha_n(V) = \frac{0.01(V+34)}{1-\exp(-0.1(V+34))}$	$\beta_n(V) = 0.125\exp(-(V+44)/80)$

2.2 Principle of TMAS on neural stimulation

The principle of TMAS is a low-intensity focused ultrasound waves moves charged ions in the brain tissue. Combined with the magnetostatic field, the ions move accelerated by a Lorentz force and form an induced electric current I_{TMAS} which is perpendicular to the direction of the magnetostatic field and the propagation of ultrasound wave, which can be written as the vector expression: $\boldsymbol{E} = \boldsymbol{V} \times \boldsymbol{B}$. Therein, $\boldsymbol{E}$ is the equivalent electrical field, $\boldsymbol{V}$ is the velocity of longitudinal particle motion of an ultrasonic wave in the medium, and $\boldsymbol{B}$ is the static magnetic field. Based on the priori knowledge, the principle of ultrasound propagation, the ion movement, and the Lorentz force could be achieved according to Montalibet's theory [37]. More detail could be found in Ref. [37]. The schematic of TMAS principle is shown in Fig. 1(a). Based on pioneering research of TMAS, the relationship between and among the ultrasonic intensity I_0, the ultrasonic fundamental frequency f_0, the magnetostatic fields intensity B_x and the electric current density J_y can be expressed as [37][38]:

$$J_y \approx \sigma B_x \sqrt{\frac{2I_0}{\rho c_0}} \sin(2\pi f_0 t) \tag{2}$$

From the Eq. (2) we could observe that J_y is produced by the electro-magnetic induction. The unit of J_y is $\mu\mathrm{A/cm^2}$. Therefore, we assign the value of J_y to the induced electric current which is regarded as an external stimulus of the neuronal network, i.e., the induced electric current I_{TMAS}. $\sigma = 0.5\mathrm{S/m}$ is the conductivity of the tissue of background, $c_0 = 1540\mathrm{m/s}$ is the ultrasound speed in the background medium. Therein, the relationship between the ultrasonic intensity I_0 and the maximum acoustic pressure P can be depicted as [38][39]:

$$I_0 = \frac{1}{2}\frac{P^2}{\rho c_0} \tag{3}$$

where ρ is the tissue density.

2.3 Numerical implementation of TMAS

The schematic diagram of the TMAS system for hippocampal neuronal network is illustrated in Fig. 1. According to the principle of TMAS, we need to produce a low-intensity focused ultrasound wave that can reach to the target position at first. We use MRI data from the standard head model in Brainstorm (https://neuroimage.usc.edu/brainstorm), a collaborative open application to analysis of brain recordings. The anatomy template in Brainstorm we used is ICBM125 2009c (https://nist.mni.mcgill.ca/icbm-152-nonlinear-atlases-2009/). The anatomical data from MRI has the real meaning, i.e., in a three-layer brain medium including scalp, skull and brain tissue in Fig. 1(b) (the average thicknesses for each layer are labeled in Fig. 1(b)), the central hippocampus locates at the 26mm right and 119mm below from the center focused ultrasound stimulation transducer. We use MRI data to design the focused ultrasound transducer and simulation experimental area. Therefore, the numerical simulation area of pressure distribution is $60\text{mm} \times 60\text{mm} \times 130\text{mm}$, and the acoustic axis is the z-axis, which satisfies the real location. We employ k-wave (http://www.k-wave.org/), an open-source MATLAB toolbox, to simulate the propagation of acoustic waves in the three-layer brain medium [40]. The more detail parameter setting could be found in Ref. [40]. The acoustical properties of tissues in numerical three layers is given in Table 2. We consider a single element bowel-shaped focused transducer with bowl radius of curvature is 130mm and bow aperture diameter 130mm (as shown in Fig. 1(c)). Moreover, the initial ultrasonic fundamental frequency $f_0 = 0.7\text{MHz}$, the focal pressure $p_F = 0.07\text{MPa}$, and the ultrasound focus hippocampus is located at 119mm from the midpoint of the computational domain. From these numerical settings, we could obtain the maximum acoustic pressure P in Eq. (3). Then, we consider the magnetostatic field intensity B_x varies from 0.05T to 1T. Combing the effects of magnetostatic field with the procedure of produce a low-intensity focused ultrasound waves, we get the electric current density J_y according to Eq. (2).

In addition, previous studies demonstrated that both continuous and modulated ultrasound waves can be used for modulating brain areas safely [41]. In our research, we consider two kinds of modulated TMAS

currents, one is a continuous ultrasound wave modulated by a sine wave, and the other one is modulated by a pulse wave. The modulation frequency MF has a range from 0.5Hz to 10Hz. Thus, the modulation TMAS currents can be explained as [28]:

$$J_y \approx \sigma B_x \sqrt{\frac{2I_0}{\rho c_0}} (\sin(2\pi(MF)t) \times (\sin(2\pi f_0 t) + 1)) \quad (4)$$

which is modulated by a sine wave, and

$$J_y \approx \sigma B_x \sqrt{\frac{2I_0}{\rho c_0}} ((\text{square}(2\pi(MF)t, Duty)) \times (\sin(2\pi f_0 t) + 1)) \quad (5)$$

which is governed by a pulse wave. Here the duty cycle $Duty$ is equal to 50%. In our study, the modulated TMAS currents are inject to each pyramidal cells and interneurons as electrical perturbation equally.

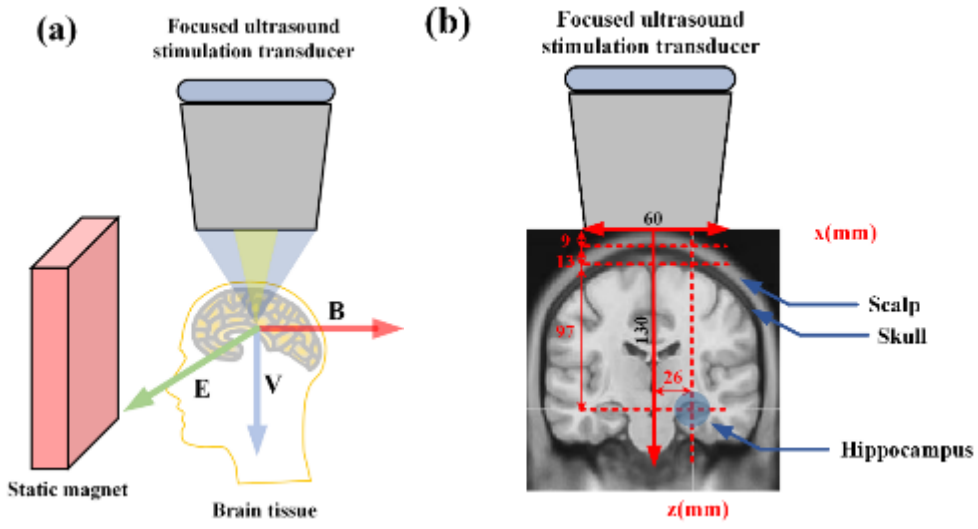

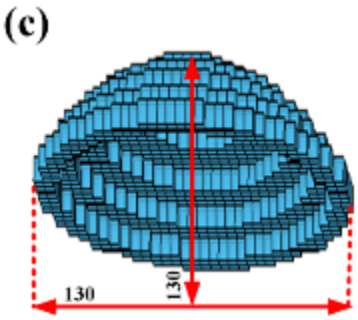

Fig. 1. (Color online) (a) The configuration of TMAS principle. (b) The locations of the focused ultrasound stimulation transducer, three layers (scalp, skull and brain tissue), and hippocampus. The dimensions in (b) are from the real MRI data. (c) Specification of the focused ultrasound stimulation transducer. The single element bowel-shaped focused transducer with bowl radius of curvature is 130mm and bow aperture diameter 130mm.

TABLE 2 Numerical simulation constant parameters [27]

Tissue	Sound speed c (m/s)	Density ρ (kg/m^3)	Acoustic absorption coefficient α (dB/cm MHz)
Scalp	1537	1116	0.85
Skull	2652	1796	4.11
Brain	1500	1000	0.10

3 Results

3.1. Features of the network configurations

In this section, we test how specific changes to the hippocampal network topology and neuronal inherent characteristics cause transition from normal to epileptic activity. Fig. 2 illustrates the plane connection matrices between hippocampal network neurons with different probability p and the nearest neighbor number K. Cell indexes from No.1 to No. 200 are the interneurons, and No. 201 to No.1000 are the pyramidal cells. In the most left column in Fig. 2 ($p = 0.1$), there are three dominant coupling types: the self-connection ranks first, the nearest-neighbor connection ranks second, and the long-distance connection ranks third. In Fig. 2(a1), the network behaves as a regular network. Few spare connections are employed to rewire neurons. By increasing the nearest neighbor number K from 50 to 450 (Fig. 2(a2)

and (a3)), next-nearest-neighbor connections appear along the diagonal, at the top left and lower right corner appear. Also, few sparse random connections are added to the network. The neuronal nodes are closely connected at first, then more sparsely the bigger K gets. More connections are broken and replaced by long-distance connections at more random locations. Synaptic connections between and among neurons are replaced by long-distance connections.

The middle column in Fig. 2 demonstrates connection matrices as $p = 0.5$. Note that the density of self-connection and nearest-neighbor connection are getting lower compared to $p = 0.1$. More random connections contribute to the network assembly. In addition, similar conclusion about the appearance of nearest-neighbor connections and long-distance connections with increased K can be seen in Fig. 2(b1) to (b3).

For the rightmost column in Fig.2, p is increased to 0.9, i.e., the higher rewiring probability shapes a more random network. Both the density of the self-connection and the nearest-neighbor connection are decreased. Random connections are dominant and thus neurons are widely randomly coupled when $p = 0.9$. The core neurons are more densely connected comprising short, medium, and long distance connections. Using these features of the network structure, we produce the epileptogenic network and investigate the dynamic mechanisms underlying seizures.

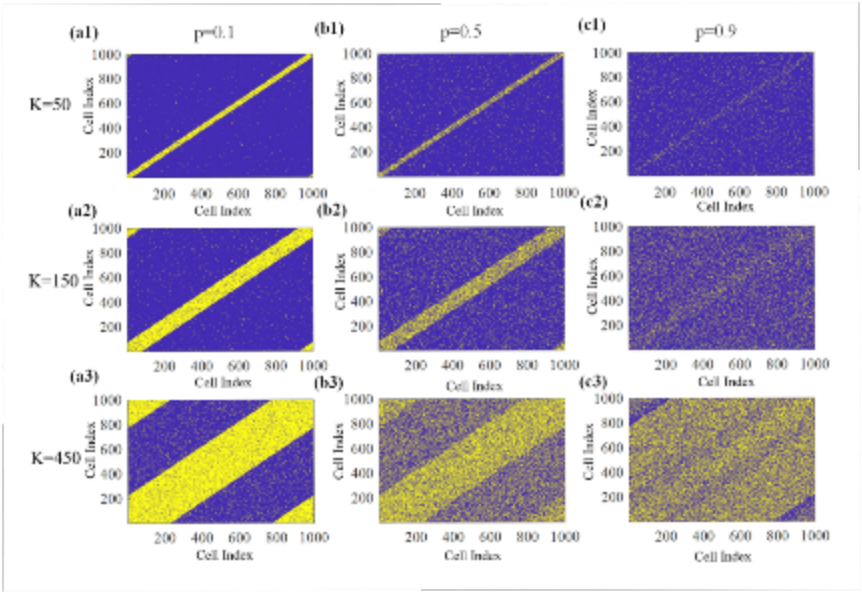

Fig. 2. (Color online) Connection matrix with topology determined by the probability p and the nearest neighbor number K. The yellow dots indicate that there is a connection ("1") between two nodes, and blue dots ("0") otherwise. Cell indexes from No.1 to No. 200 are the interneurons, and No. 201 to No.1000 are the pyramidal cells. The columns from left to right are organized as $p = 0.1, 0.5$ and 0.9, respectively. The rows from upper to lower are correspond to $K = 50, 150$ and 450, respectively. The horizontal and vertical coordinates denote the cell index.

3.2. Dynamical properties of the epileptic hippocampal network

Combining previous research on network topology with the studies of epileptiform activities *in vitro*, we construct the epileptic network to investigate the dynamical properties of the epileptic hippocampal network. By changing network topology and neuronal inherent parameters, we first reproduce the complete epileptic dynamics transitions from slow interictal discharges, ictal discharges, then to postictal activity [14] Fig. 3(a1) presents the stimulated local field potentials (LFPs) for 50s corresponding to the hippocampal area. From Fig. 3(a) we reproduce the slow interictal discharge (green background) which is a kind of synchronized activity (the synchronization is examined in Fig. 3(b3)) with a duration of about 10s. It is known to originate from the entorhinal cortex (EC) and propagate to other subareas of the hippocampus [42] [43]. The sporadic spiking at a frequency of 1~3Hz with an amplitude of about 100μV are a typical time-frequency feature of slow interictal discharges. In addition, they are frequently observed before ictal onset discharges. The ictal discharges are highlighted by the blue background. The seizure-like event lasts about 28s with a dominant frequency of about 15Hz. Sustained irregular spike waves can be found during the seizures. The last phase is the postictal discharge pattern which is highlighted by the light yellow background. Following ictal discharges, the whole network is in a saturated state and thus the postictal discharges have a small amplitude during that phase. Fig. 3(a2) is a detail of clinical scalp electroencephalogram recording for right posterior temporal, which contains the hippocampal area. Comparing Fig. 3(a1) with (a2), we clearly observe that the simulation results show similar shape and rhythm to clinical recording.

Next, we show time series and spike raster diagrams of individual neurons corresponding to the three typical discharge patterns. Experimental observations show that epileptiform activities could be induced by increasing the extracellular concentration of potassium ions and the inherent external input, here we consider the potassium ion potential $V_{K_{ex}}$ and the external current input for the excitatory cell I_e are crucial parameters. Fig. 3(b1) to (b3) demonstrate time series and spike raster diagram of excitatory pyramidal cells and inhibitory interneurons with parameters $K = 200, p = 0.1, I_e = 0.3\mu\mathrm{A/cm}^2, V_{k_{ex}} = -75\mathrm{mV}$. All neurons show synchronized spiking discharges. We then reproduce the ictal discharge (Fig. 3(c1) to (c3)) and postictal discharges (Fig. 3(d1) to (d3)) by changing the critical parameters, respectively. For the ictal discharge state, the synchrony of pyramidal cells is a bit of lower than during slow interictal discharge and the interneurons show synchronized bursting discharges as $K = 200, p = 0.5, I_e = 0.3\mu\mathrm{A/cm}^2, V_{k_{ex}} = -100\mathrm{mV}$. For the postictal discharge, the interneurons show synchronized fast rhythmic activity, while the pyramidal neurons demonstrate oscillations with small-amplitude as $K = 50, p = 0.1, I_e = 0.2\mu\mathrm{A/cm}^2, V_{k_{ex}} = -50\mathrm{mV}$.

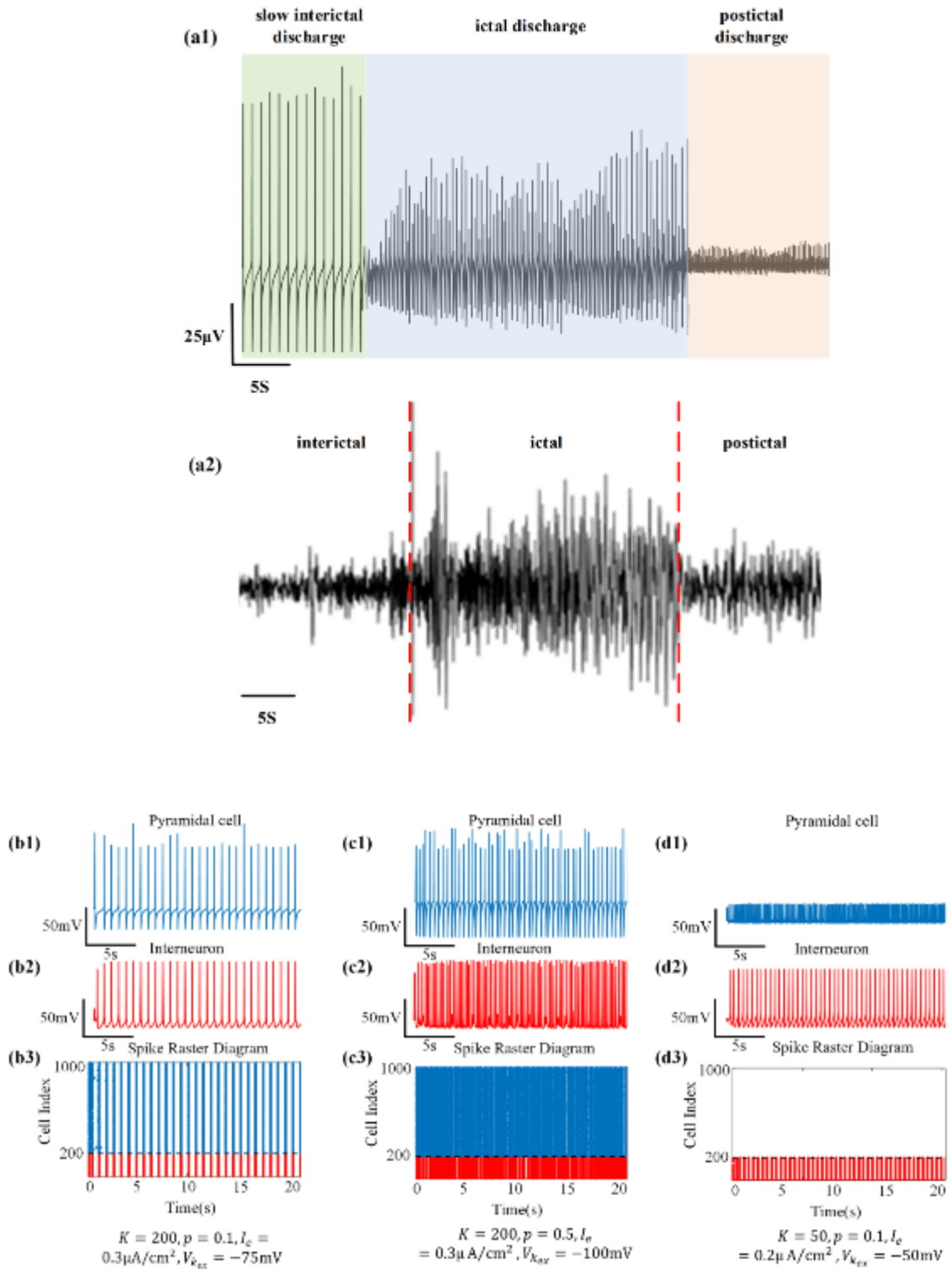

Fig. 3. (Color online) Epileptiform activities produced by the hippocampal network model. (a1) Time series includes the slow interictal discharge (green shadow), the ictal discharge (blue shadow) and the postictal discharge (light yellow shadow). (a2) is clinical recording in a patient with drug-resistant epilepsy. Here T6 channel is shown as an example. The data was obtained from Sanbo Brain Hospital of Capital Medical University in Beijing. The

electroencephalography (EEG) was recorded with a Nicolet video-EEG monitoring system (Thermo-Fisher Scientific, Waltham, MA, USA) and digitized at a rate of 512Hz with the international standard 10-10 electrode montage. The online band-pass filter was preset to 1.6-150Hz. (b1) to (b3), (c1) to (c3) and (d1) to (d3) illustrate the respective epileptic oscillatory activities. (b1), (c1) and (d1) represent time plots for the pyramidal cell as $K = 200, p = 0.1, I_e = 0.3\mu A/cm^2, V_{k_{ex}} = -75mV$, $K = 200, p = 0.5, I_e = 0.3\mu A/cm^2, V_{k_{ex}} = -100mV$ and $K = 50, p = 0.1, I_e = 0.2\mu A/cm^2, V_{k_{ex}} = -50mV$, respectively. (b2), (c2) and (d2) represent time plots for the interneuron in the same condition with the above panel. (b3), (c3) and (d3) are the corresponding spike raster diagrams of the network.

These plots in Fig. 3 illustrate that the basic pyramidal-interneuron hippocampal network has the capability to produce typical epileptic discharge from the point of view of the LFP. However, is essential to quantify the influence of crucial parameters including the network topology (K and p) features and the neuronal inherent characteristics (I_e and $V_{K_{ex}}$) on the dynamics. Here, we first to explore the influence of K and p in terms of the neuronal state with fixed I_e and $V_{K_{ex}}$. There are four states of the neurons: the oscillations with small-amplitude (1) (typical time series is shown in Fig. 3(d1)), the synchronized spiking discharge (2) (typical time series are shown in Figs. 3(b1) and (b2)), the desynchronized spiking discharge (3) (typical time series is shown in Fig. 3(c1)) and the synchronized bursting discharge (4) (typical time series is shown in Fig. 3(c2)). Fig. 4(a) shows the parameter space of pyramidal cell by designing various network topologies with fixed I_e and $V_{K_{ex}}$, from which we see that the pyramidal cell is in the synchronized spiking state when K is smaller than 300 and p is smaller than 0.6. By increasing K and p together, we find the pyramidal cell transit to the desynchronized spiking state. We find similar dynamical transition pattern in the parameter space of interneurons, so we only demonstrate the situation of pyramidal cell. Next, consider two typical types of network structures: one is when the self-connection ranks first and the network behaves as a regular network (connection matrix shown in Fig. 2(a1)), and the other one is when long-distance connections are in the dominant position and the network topology tends to a random configuration (connection matrix is similar to Fig. 2(b2)).

For the former (results are shown in Fig. 4(b1) and (b2)), the pyramidal cells demonstrate oscillations with small-amplitude when $V_{K_{ex}}$ is not small enough, while the interneurons show synchronized spiking discharges. By decreasing $V_{K_{ex}}$, we get the synchronized spiking of pyramidal cells and the interneurons persist spiking. If we continue decreasing $V_{K_{ex}}$ to -75mV, we get the desynchronized spiking state when I_e is smaller than $0.5\mu A/cm^2$. However, the interneurons switch states from synchronized spiking to synchronized bursting discharge when I_e increases to $0.9\mu A/cm^2$. For the later one (results are shown in Fig. 4(c1) and (c2)), similar results as in Fig. 4(b1) and (b2)) could be found in both the pyramidal cells and interneurons by regulating $V_{K_{ex}}$. Note that the state of desynchronized spiking in pyramidal cells also appears when I_e increases to $0.9\mu A/cm^2$ and $V_{K_{ex}}$ decreases to -85mV. In comparison to Fig. 4(b2), the interneurons will transit early to the state of synchronized bursting when I_e increases to $0.7\mu A/cm^2$. In conclusion, the two-dimensional parameter spaces with K and p and with I_e and $V_{K_{ex}}$, respectively, provide structural proofs for essential dynamical state transitions of the epileptic hippocampal network.

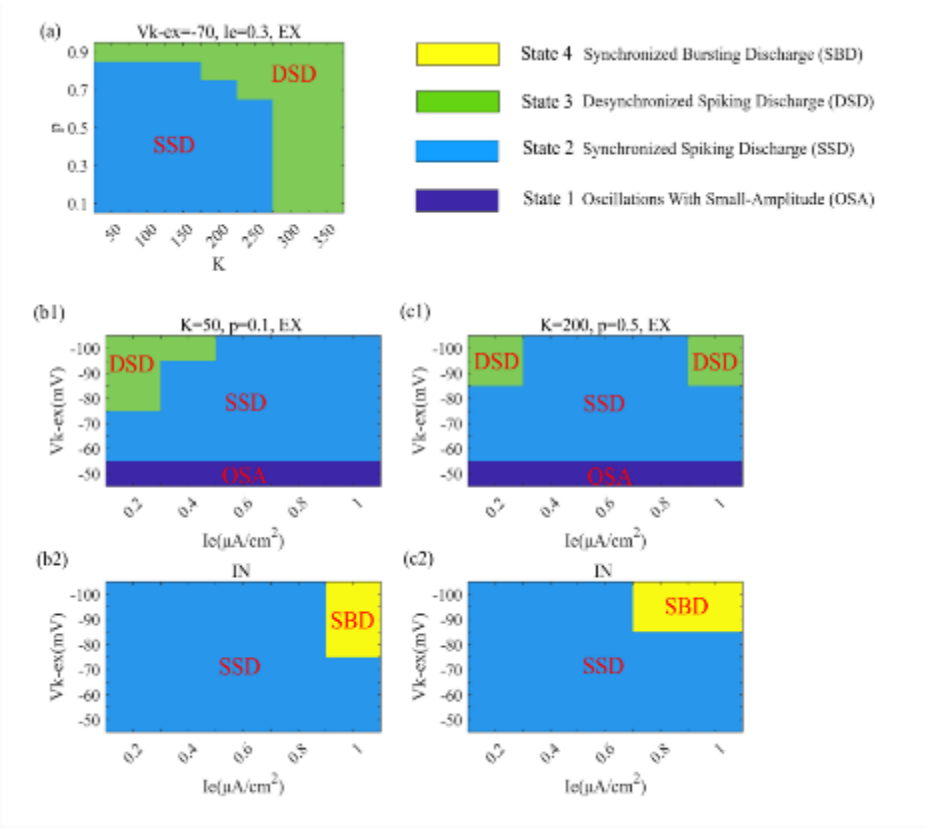

Fig. 4. (Color online) Parameter spaces for neuronal transition states in two dimensions. (a) demonstrates the two-dimensional structural network parameter (K and p) diagram for pyramidal cells. The four states (shown in colorbars) considered are the oscillations with small-amplitude (OSA) (1), the synchronized spiking discharge (SSD) (2), the desynchronized spiking discharge (DSD) (3) and the synchronized bursting discharge (SBD) (4). (b1) to (b2) and (c1) to (c2) are two-dimensional neuronal inherent parameter (I_e and $V_{K_{ex}}$) diagrams for pyramidal cells and interneurons, respectively. (b1) and (b2) are plotted as $K = 50$ and $p = 0.1$, while $K = 200$ and $p = 0.5$ are for (c1) and (c2).

3.3. Exploring the effects of TMAS modulation strategy on the epileptic hippocampal network

According to the theory of TMAS, we need to produce a low-intensity focused ultrasound wave at first. The more detail procedure of k-wave toolbox to simulate the propagation of acoustic waves and the parameter setting could be found in Ref. [40]. The acoustic source is defined to be a focused transducer driven by a continuous wave sinusoid at 0.7 MHz with a surface pressure of 0.07MPa. By employing the bowel-shaped focused transducer we designed in Fig. 1(c), we simulate the ultrasound pressure field and the distribution of ultrasonic intensity in a three-layer brain medium (shown in Fig. 1(b)), respectively. Fig. 5(a1) and (b1) show the sound pressure field for the $z - x$ panel when $z = 119\text{mm}$ and $x = 26\text{mm}$ and the $y - x$ panel when $y = 0\text{mm}$ and $x = 26\text{mm}$, respectively (these dimensions are according to the location of hippocampus area in Fig. 1(b)). It can be observed that the hippocampal area is accurately focused transcranially. Fig. 5(a2) and (b2) are the distribution of ultrasonic intensity for the z orientation ($x = 26\text{mm}$) and the y orientation ($x = 26\text{mm}$), respectively. The change curves of the sound and non-sound axis ultrasonic intensity, especially the maximum intensity, are consistent with the distribution (e.g. the focus position) of the ultrasound pressure field. These results illustrate that the transcranial focused ultrasound is well focused and has the ability to reach the position of the hippocampus. This setup lays the foundation of the subsequent movement transition from the magnetic to the electric field.

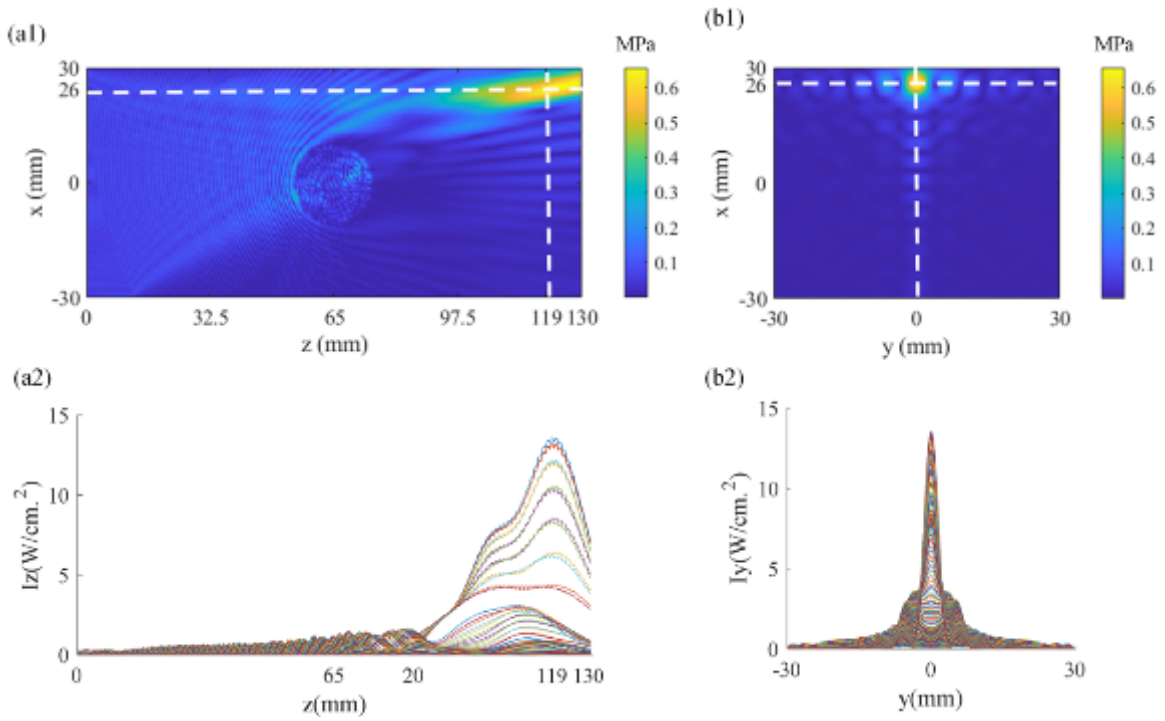

Fig. 5. (Color online) (a1) and (a2) are ultrasound pressure field distribution at $z-x$ panel ($z = 119$mm, $x = 26$mm) and $y-x$ panel (y $= 0$mm, $x = 26$mm), respectively. (a2) and (b2) are the curves of sound intensity of pulsed sinusoidal ultrasonication in z orientation ($x = 26$mm) and y orientation ($x = 26$mm), respectively.

Next, we exert the magnetostatic field to the hippocampus. The magnetostatic fields intensity B_x varies from 0.05T to 1T. Combing the effects of magnetostatic field with the focused ultrasound waves, we get the TMAS currents. Here we consider two types of modulated TMAS currents, the sine wave-modulated and the pulse wave-modulated. In our study, the modulated TMAS currents are inject to each pyramidal cells and interneurons as electrical perturbation equally.

Fig. 6 shows an example of the original induced TMAS current (a), the sine wave-modulated TMAS current (b), the sine wave (c), the pulse wave-modulated TMAS current (d) and the pulse wave (d). Here the magnetic intensity is $B_x = 0.2$T and the modulation frequency $MF = 0.5$Hz. From Fig. 6(a) we can observe that the original TMAS current is a very intensive sine wave. The sine wave-modulated TMAS current shown in Fig. 6(b) has a sine wave envelope and lower frequency compared with Fig. 6(a), while the pulse wave-modulated TMAS current in Fig. 6(d) has a pulse wave envelope

line and the same frequency a sine wave-modulated TMAS. It is worthy to note that the sine wave-modulated (Fig. 6(b)) and pulse wave-modulated rectangular TMAS pulses (Fig. 6(d)) are filled. To load the original carrier frequency signals (Fig. 6(a)) onto modulating signals (Figs. 6(c) and (e)) with a certain frequency, the TMAS pulses are produced. Details are shown from 4 to 4.005s in Figs. 6(d) and (d), respectively. The filled TMAS pulses in Figs 7 and 8 are as well.

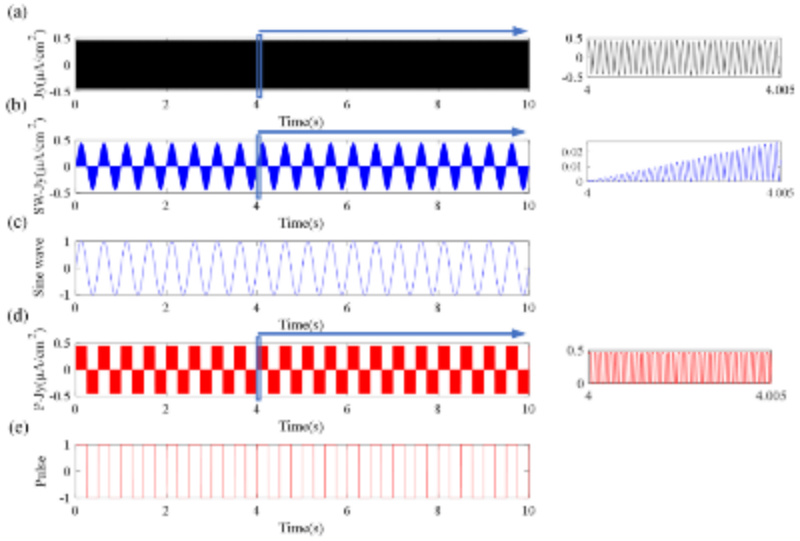

Fig. 6. (Color online) Time plots for TMAS current with different modulation signals. (a) is the original TMAS current. Detail is shown from 4 to 4.005s. (b) and (c) are the sine wave-modulated TMAS current and its modulation signal, respectively. Detail is shown from 4 to 4.005s. (d) and (e) are the pulse wave-modulated TMAS current and its modulation signal, respectively. Detail is shown from 4 to 4.005s. The filled with activity in (b) and (d) have the same meaning for Figs. 7 and 8.

Starting from the different modulation signals and their modulated TMAS currents, we investigate the characteristics of the LFP curves, modulated TMAS currents plots, and the spike raster diagrams of the network for different TMAS parameters in Figs. 7 and 8. In our control strategy, we try to prevent the network entering into the state of ictal discharge. The network is in a state of interictal discharge, postictal discharge, or periodic spiking, which suggests our control strategy is successful. In Fig. 7, the fixed parameter is $MF = 1\text{Hz}$ and the adjustable parameter B_x is from 0.1T to 1T. The initial state of the hippocampal network is the ictal discharge state and the TMAS current is injected at 10s. The settled

epileptic network structure is assembled based on the analysis in Fig. 4. Perturbation control results are presented with two kinds of modulation signals. As shown in Fig. 7(a1) to (a3), the plots of LFP slowly transits to the slow interictal discharge state at about 18s and the amplitude of the TMAS current is small. Furthermore, the control results by the pulse wave-modulated has similar transitions as shown in Fig. 7(d1) to (d3). As B_x increases to 0.4T shown in Fig. 7(b1) to (b3), a TMAS current with higher amplitude density is injected to the network and the LFP shifts to slow interictal discharge state quickly. Similar results could be also found in Fig. 7(e1) to (e2). Then, we continue increasing B_x to 1T, the outcome shown in Fig. 7(c1) to (c3). The epileptic network responds to the TMAS control as soon as the current is injected. The firing pattern of LFP changes from slow interictal discharge to the phase-locking periodic spiking pattern. In addition, Fig.7 (f1) to (f3) demonstrate that the epileptic network has a similar response to the pulse wave-modulated TMAS current under the same conditions as the sine wave-modulation. We conclude that as the magnetic density increases, the dynamics of the network will transit from the ictal discharge state to slow interictal discharge state then to the phase-locking periodic spiking state, and the corresponding speed is also increased under the two types of TMAS control strategies.

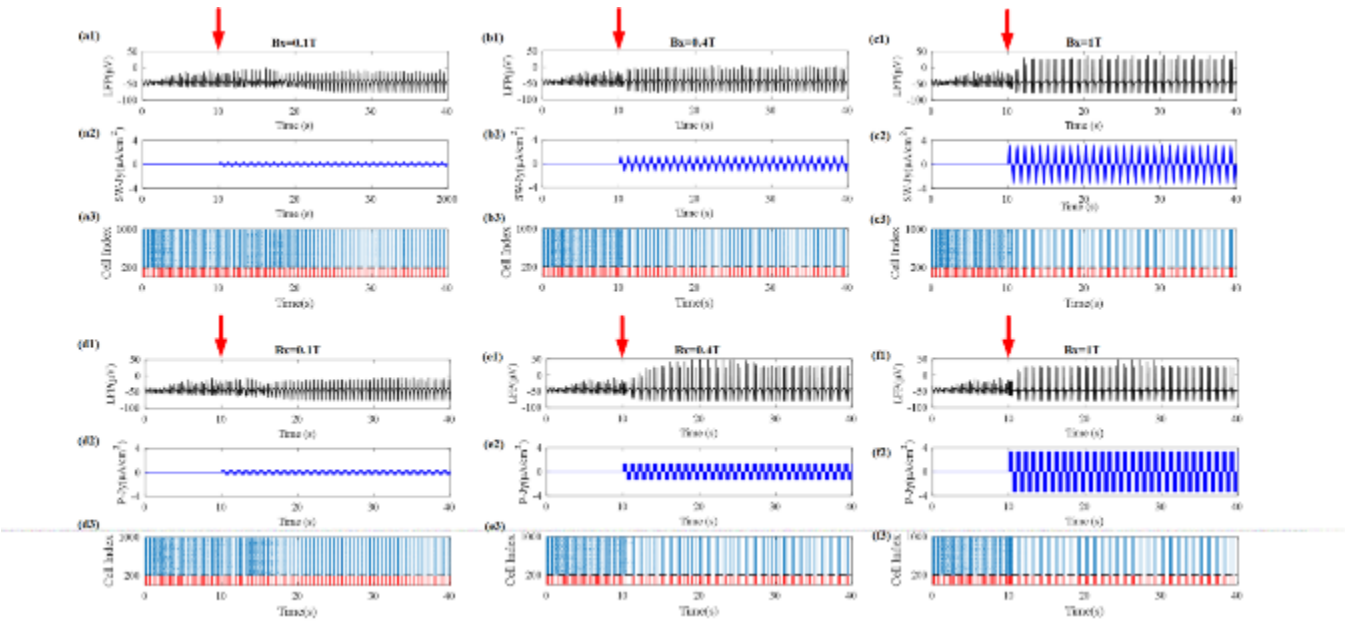

Fig. 7. (Color online) Different discharge patterns with various B_x. (a1), (a2), (a3) are time plots of LFP, sine-wave modulated TMAS current, and the spike raster diagrams of the network as $B_x = 0.1$T. (b1) to (b3) are plotted as $B_x = 0.4$T. (c1) to (c3) are described as $B_x = 1$T. (d1) to (d3), (e1) to (e3) and (f1) to (f3) are plotted under pulse wave-modulated control strategy.

Next, we analyze the response of the epileptic network to TMAS control strategy with various values of MF. The fixed parameter is $B_x = 0.2$T and the TMAS current is injected at 10s. Fig. 8(a1) to (a3) demonstrate the TMAS results by sine-wave modulation as $MF = 0.1$Hz. The epileptic network slowly responds to the TMAS and does not achieve a dynamical transition from ictal discharge to slow interictal or postictal discharge. In comparison with Fig. 8(d1) to (d3), we find that the network intends to transit to the slow interictal discharge state when the TMAS current is injected about 7s later. After that, the firing pattern of the network reaches the slow and fast mixed periodic spiking state. When increasing MF to 0.3Hz, the epileptic network responds to the TMAS current modulated by sine wave quickly and transits to the slow interictal discharge at about 13s (Fig. 8(b1) to (b3)). The LFP modulated by the pulse wave does not seem to be periodic (shown in Fig. 8(e1) to (e3)). Finally, we increase MF to 2.5Hz. Results illustrated in Fig. 8(c1) to (c3) and (f1) to (f3) show that the epileptic LFPs fail to be terminated with both types of modulated TMAS currents because the morbid rhythm is not be decreased. Therefore, the epileptic network could transit to the slow interictal discharge state as the modulation frequency MF increases to a proper value.

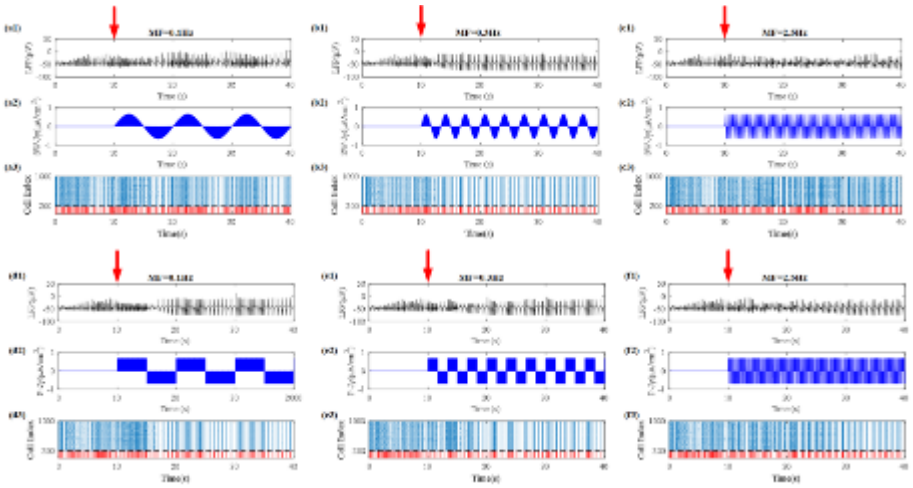

Fig. 8. (Color online) Different discharge patterns with different MF. (a1), (a2), (a3) are time plots of LFP, sine-wave modulated TMAS current, and the spike raster diagrams of the network as $MF = 0.1Hz$. (b1) to (b3) are plotted as $MF = 0.3$Hz. (c1) to (c3) are described as $MF = 2.5$Hz. (d1) to (d3), (e1) to (e3) and (f1) to (f3) are plotted under the pulse wave-modulated control strategy.

Furthermore, we quantitatively investigated the interspike interval (ISI) bifurcation diagrams of the epileptic network under the two types of TMAS modulation strategies. The transitions for neurodynamic are usually illustrated by means of ISI bifurcation of stable bursting orbits as one parameter changes[44]. This kind of diagrams presents various cascades of period or chaotic phenomena. In this study, ISI is calculated from the sampled series for LFP. Fig. 9(a1) and (b1) show ISI bifurcation diagrams of parameter B_x ($MF = 0.1$Hz) under both stimulation strategies. It is observed in Fig. 9(a1) that the epileptic network shows ictal discharges before reaching the bifurcation point at around $B_x = 0.4$T, then transits to the phase-locking periodic spiking state. A similar transition can be seen in Fig. 9(b1) under the pulse-modulated stimulation. Here, the epileptic network transits to the other state earlier than under the above strategy, i.e., the bifurcation point is earlier than the above. Fig. 9(a2) and (b2) are ISI bifurcation diagrams of MF ($B_x = 0.2$T). In Fig. 9(a2), the epileptic network seems to be very stable at the ictal state and slowly transits to the slow interictal discharge state by increasing MF, and finally gets to be chaotic. In terms of the pulse-modulated case, the epileptic network responses to the TMAS is more active. However, the epileptic network is slightly chaotic eventually.

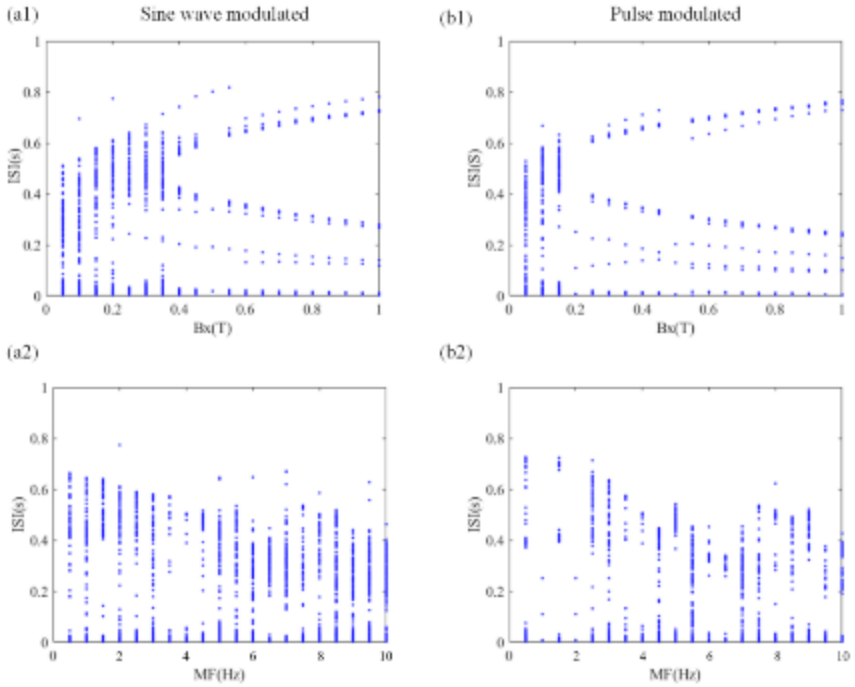

Fig. 9. (Color online) Analysis of dynamical transitions for the epileptic hippocampal network under different modulation parameters. (a1) and (a2) are illustrations of ISI bifurcation diagrams under sine wave-modulated TMAS. The modulation parameters are B_x (a1) and MF (a2), respectively. (b1) and (b2) are ISI bifurcation diagrams modulated by the pulse wave. B_x (b1) and MF (b2), respectively.

To further make comparisons between different TMAS strategies considering modulation modes and regulatory parameters, we calculate the energy of the TMAS current for each trial (conditions are settled in Fig. 9). The energy can be obtained as $\text{Energy} = \int_0^T |J_y|^2 \, dt$ where T is the total trial time. We also mark the valid point (begin) and the invalid point (end) for the modulation strategy. From Fig. 10 we observe that in the control valid regions the epileptic network needs more energy to accomplish transitions by increasing B_x, and that the sine wave-modulated strategy needs less energy. In terms of the modulation strategy by regulating MF, the sine wave-modulated TMAS strategy also consumes less energy, but this strategy has small control valid region in comparison with the B_x driven strategy. In general, the MF driven modulation strategy shows better energy efficiency.

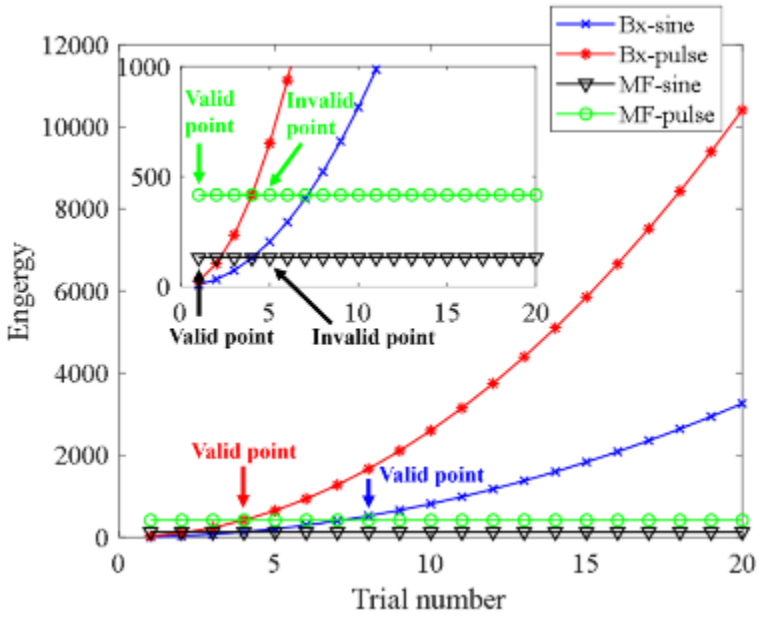

Fig. 10. (Color online) Energy variation of different TMAS modulated strategies. The green line with circles represents the MFdriven pulse wave modulated strategy, the black line with triangles illustrates the MFdriven sine wave modulated strategy, the red line with stars demonstrates the B_x driven pulse wave modulated strategy, and the blue line with forks denotes the B_x driven sine wave modulated strategy. The detailed drawing shows the vertical coordinate for the energy is from 0 to 1000. The blue arrow indicates the valid point begin from the eighth trial for B_x driven pulse wave and the red arrow indicates the valid point begin from the fifth trial for B_x driven sine wave, respectively. There are no invalid points under these two strategies. The left and right black arrows present the valid point begin from the first trail and end at the fifth trail (the invalid point) for MFdriven sine wave, respectively. The left and right green arrows present the valid point begin from the first trail and end at the fifth trail (the invalid point) for MFdriven pulse wave, respectively.

4. Discussion and Conclusions

In this work, we proposed a comprehensive hippocampal computational network model that reproduces epileptiform activities including slow interictal discharge, ictal discharge and postictal discharges and investigated dynamical mechanisms underlying epileptic activities and different TMAS strategies. We first explored the effects of network configurations on the dynamical mechanisms. We employ the Olufsen model and the Wang and Buzsáki (WB) model, two types of Hodgkin-Huxley like neuronal computational models, to represent pyramidal cell and interneuron cell, respectively. Neurons

are assembled based on the small-world network structure. By deriving a variety of network structures, we analyse the influence of structural parameters on the network dynamics. By increasing the probability p and we demonstrate the network tends to be more random. As the nearest neighbor number K is increased, the nearest-neighbor connections appear first and long-distance connections dominate later. In terms of the graph structure, neurons distribute sparsely at first, and then connect in a more focused way due to the wide-spread long-distance connections.

Based on the understanding of the network dynamics, we form the epileptic hippocampal network combining the structural parameters and neuronal inherent parameters (the potassium ion potential and the external current input of the pyramidal cell). Usually, epileptic events arise due to the interaction between relatively fast neuronal excitation and comparatively slower ion dynamics [45]. Especially, an increase of extracellular potassium concentration is observed during the epileptiform bursting. Researches also demonstrated the generation and persistence of epileptic seizure is affected by the extracellular potassium changes [46]. In our study, the variation of reversal potential of potassium is in accordance with the instantaneous changes of extracellular potassium concentration by Nernst equation [45], which shows slow dynamics. In contrast, the membrane potential demonstrates relative fast activity. In addition, the currents including inhibitory postsynaptic current mediated by GABAergic dynamics, the external inputs and the TMAS currents are essential to maintain the balance of intra and extra potassium concentration and potassium currents. Thus, our study could reduce a complete ictal discharge, repeating ictal discharges, and transitions between ictal and interictal discharge. In more detail, we will consider the specific potassium and pump, glia, and diffusion dynamics in the future research.

We find that the influences of the pyramidal cells including their inherent and structural parameters could induce transitions from interictal to ictal discharges and then to postictal discharges. The activities of individual neurons and the synchronization of the network as a function of these parameters were described. Furthermore, the two-dimensional parameter space in Fig. 4 provides a quantitative way to

identify the respective dynamical states and the corresponding transitions. Here we take the size of 1000 neurons as an example. In the research of Howe et al [47], they construct a CA3 network with 240 basket cells and 1200 pyramidal cells and a CA1 network with 160 basket cells and 800 pyramidal cells, respectively. They employ these hippocampal networks to study the effect of NMDA receptors on sharp-wave ripples, and the size in this paper which is similar to our research, representing a proper size for a small hippocampus area in the real mammalians brain. Thus, the network scale we choose is reasonable. We also test the results with the number of neurons changing from 200 to 2000 (interval is 200). We find the results are robust. However, the network scale in our research is still small, we still need to test the efficiency in large scale network (N>10000) and more hippocampal areas.

Various experiments [48] [49] have demonstrated the feasibility of TMAS in neuromodulation. In this work, the k-wave is employed to simulate the propagation of a continuous acoustic wave. The single element bowel shaped focused transducer is designed based on the numerical simulation area which reflects a real distribution of the three-layer brain medium and the location of the hippocampus. We demonstrated that the focused ultrasound system has the ability to transcranially target the hippocampal area accurately. Based on the advanced TMAS techniques, we investigated two kinds of modulated TMAS strategies to suppress seizures. Strategies based on magnetic intensity were tested in Fig. 7. The epileptic network could transit from the ictal discharge to the phase-locking periodic spiking by increasing the magnetic intensity and the network more actively responds to the pulse-wave modulated TMAS strategy. However, the two modulation methods based on the modulation frequency seems not to be able to terminate seizures activity. The epileptic network could transit to the slow interictal discharge state only when the modulation frequency is settled within a specific range. Also, observations from the ISI bifurcation diagrams in Fig. 9 confirmed the above conclusions. In this paper, we concentrate on analysing the effects of TMAS on the whole network and don't provide dynamical bifurcations of single neurons. In our another paper, we calculate the ISIs of pyramidal cell and interneuron to study the effects of TMAS on neuronal nonlinear dynamical properties at different magnetic field intensities and

use the maximum ISI of neurons after TMAS as an indicator of epileptic latency. We quantitatively identified three bifurcation points for state transitions by changing the magnetic field strength. The results indicate that TMAS can increase the latency of hypersynchronous seizures and eventually result in the transition to the resting state at sufficient intensity. Finally, the energy consumption for all trials are calculated to quantificationally evaluate the neuromodulation performance. The pulse wave-modulated TMAS strategy based on magnetic intensity shows the best performance in suppressing seizures but requires maximum energy. The strategy based on sine wave-modulated TMAS using magnetic intensity ranks second and needs less energy. Although, strategies based on modulation frequency are energy saving, their performance in terminating seizures are the worst. From the comparisons above, the TMAS strategy based on magnetic intensity is the most efficient for seizure termination. With reference to ultrasonic fundamental frequency ($f_0 = 1$MHz VS 0.7MHz) and intracranial ultrasound stimulation pressure ($p_F = 3$MPa VS 0.07MPa) in Ref.[29], and modulation frequency (MF varies from 5 to 150Hz VS 0.5Hz to 10Hz) in Ref.[28], we set the TMAS parameters in our paper. Besides, for the sake of safety, our magnetic field intensity (B_x varies from 0.05T to 1T) is also within the parameter range required for diagnosis. These parameters design is reasonable. Our paper provides theoretical exploration evidences on TMAS for suppression of seizures, however, the accuracy of stimulation parameters should be tested in further eletrophysiological experiments.

The limitations in this work are: 1) We need to consider more network structures with various numbers of neurons to strengthen the reliability of this work. 2) This work only considers the local stimulation effects of the induced TMAS current. The spatial distribution stimulation effect should be considered in the future research. 3) We consider the interaction of two stimulation parameters at first, but we find that the modulation frequency has a very narrow modulation range and the magnetic field intensity acts dominantly in suppressing seizures. We will sake for other superior stimulation parameters, e.g., the spatial-peak temporal-average intensity (I_{spta}) and spatial-peak-pulse-average intensity (I_{sppa}). Our research provides a comprehensive view to assess the efficiency for different

TMAS strategies together with their underlying mechanisms in a detailed computational model of the epileptogenic hippocampus. Our results enrich the theoretical basis of epileptic dynamics and its potential non-invasive control and we hope that such work will helpful for future clinical treatments of neurological disorders.

Author contribution

Liyuan Zhang: Conceptualization, Methodology, Software, Writing original draft, Writing-reviewing & editing. **Yuejuan Xu**: Designed, Performed the research, Analyzed the data, Writing the original draft. **Gerold Baier:** Conceptualization, Methodology, Writing-reviewing & editing. **Youjun Liu:** Conceptualization, Writing-reviewing. **Bao Li:** Conceptualization, Methodology, Software, Writing-reviewing & editing.

Declaration of competing interest

The authors declare that they have no known competing financial interests or personal relationships that could have appeared to influence the work reported in this paper.

Data availability

The data that support the findings of this study are available from the corresponding author upon reasonable request.

Funding

This research was supported by the National Natural Science Foundation of China (Grant Nos. 12102014, 11932003, 32271361 and 12202022) and the National Key Research and Development Program of China (Grant Nos. 2021YFA1000200 and 2021YFA1000202).

References

[1] Haut, S.R. and Nabbout, R.. Recognizing seizure clusters in the community: The path to uniformity and individualization in nomenclature and definition. Epilepsia 63(Suppl.1): S6-S13 (2022). https://doi.org/10.1111/epi.17346

[2] Sainburg, L.E., Janson, A.P., Johnson, G.W., et al. Structural disconnection relates to functional changes after temporal lobe epilepsy surgery. Brain awad117(2023). https://doi.org/10.1093/brain/awad117

[3] Bernhardt, B.C., Bonilha, L. and Gross, D.W. Network analysis for a network disorder: The emerging role of graph theory in the study of epilepsy. Epilepsy Behav 50:162-170(2015). https://doi.org/10.1016/j.yebeh.2015.06.005

[4] Voets, N.L., Beckmann, C.F., Cole, D.M., et al. Structural substrates for resting network disruption in temporal lobe epilepsy. Brain 135:2350-2357(2012). https://doi.org/10.1093/brain/aws137

[5] Watts, D.J. and Strogatz, S.H. Colletive dynamics of 'small-world' networks. Nature 393(4):440-442(1998). https://doi.org/10.1038/30918

[6] Netoff, T.I., Clewley, R., Arno, S., et al. Epilepsy in small-world networks. J Neurosci 24(37):8075-8083(2004). https://doi.org/10.1523/JNEUROSCI.1509-04.2004

[7] Percha, B., Dzakpasu, R. and Żochowski, M. Transition from local to global phase synchrony in small world neural network and its possible implications for epilepsy. Phys Rev E 72:031909(2005). https://doi.org/10.1103/PhysRevE.72.031909

[8] Scharfman, H.E. The enigmatic mossy cell of the dentate gyrus. Nat Rev Neurosci 17:562-575(2016). https://doi.org/10.1038/nrn.2016.87

[9] Shiri, Z., Manseau, F., Lévesque, M., et al. Activation of specific neuronal networks leads to different seizure onset types. Ann Neurol 79(3):354-365(2016). https://doi.org/10.1002/ana.24570

[10] Cordon, T. and English, A.W. Strategies to promote peripheral nerve regeneration: Electrical stimulation and/or exercise. Eur J Neurosci 43(3): 336-350(2016). https://doi.org/10.1111/ejn.13005

[11] Zhang, L., Fan, D. and Wang, Q. Synchronous high-frequency oscillations in inhibitory-dominant network motifs consisting of three dentate gyrus-CA3 systems. Chaos 28:063101(2018). https://doi.org/10.1063/1.5017012

[12] Zhang, L., Ma, Z., Yu, Y., et al. Examining the low-voltage fast seizure-onset and its response to optogenetic stimulation in a biophysical network model of the hippocampus. Cogn Neurodynamics (2023). https://doi.org/10.1007/s11571-023-09935-1

[13] Yu, Y., Han, F. and Wang, Q. A hippocampal-entorhinal cortex neuronal network for dynamical mechanisms of epileptic seizure. IEEE T Neur Sys and Reh 31:1986-1996(2022). https://doi.org/10.1109/TNSRE.2023.3265581

[14] Ahn, S., Jun, S.B., Lee, H.W., et al. Computational modeling of epileptiform activities in medial temporal lobe epilepsy combined with in vitro experiments. J Comput Neurosci 41:207-223(2016). https://doi.org/10.1007/s10827-016-0614-8
[15] Wendling, F., Benquet, P., Bartolomei, F., et al. Computational models of epileptiform activity. J Neurosci Meth 260:233-251(2016). https://doi.org/10.1016/j.jneumeth.2015.03.027
[16] Curia, G., Longo, D., Biagini, G., et al. The pilocarpine model of temporal lobe epilepsy. J Neurosci Meth 172:143-57(2008). https://doi.org/10.1016/j.jneumeth.2008.04.019
[17] Yu, Y., Hao, Y. and Wang, Q. Model-based optimized phase-deviation deep brain stimulation for Parkinson's disease. Neural Networks 122:308-319(2019). https://doi.org/10.1016/j.neunet.2019.11.001
[18] Ben-Menachem, E. Vagus-nerve stimulation for the treatment of epilepsy. Lancet Neurol 1: 477-482(2002). https://doi.org/10.1016/S1474-4422(02)00220-X
[19] Yang, A-C., Shi, L., Li, L-M., et al. Potential protective effects of chronic anterior thalamic nucleus stimulation on hippocampal neurons in epileptic monkeys. Brain Stimul 8: 1049-1057(2015). https://doi.org/10.1016/j.brs.2015.07.041
[20] Krook-Magnuson, E., Szabo, G.G., Armstrong, C., et al. Cerebellar directed optogenetic intervention inhibits spontaneous hippocampal seizures in a mouse model of temporal lobe epilepsy. eNeuro 1(1):e.2014(2014). https://doi.org/10.1523/ENEURO.0005-14.2014
[21] Regner, G.G., Pereira, P., Leffa, D.T., et al. Preclinical to clinical translation of studies of transcranial direct-current stimulation in the treatment of epilepsy: a systematic review. Front Neurosci 12:189(2018). https://doi.org/10.3389/fnins.2018.00189
[22] Rabut, C., Yoo, S., Hurt, R.C., et al. Ultrasound technologies for imaging and modulating neural activity. Neuron 108:93-110(2020). https://doi.org/10.1016/j.neuron.2020.09.003
[23] Brinker, S.T., Preiswerk, F., White, P.J., et al. Focused ultrasound platform for investigating therapeutic neuromodulation across the human hippocampus. Ultrasound Med Bio 46(5): 1270-1274(2020). https://doi.org/10.1016/j.ultrasmedbio.2020.01.007
[24] Zhang, H., Yu, Y., Deng, Z., et al. Activity pattern analysis of the subthalamopallidal network under ChannelRhodopsin-2 and Halorhodopsin photocurrent control. Chaos Soliton Fract 138:109963(2020). https://doi.org/10.1016/j.chaos.2020.109963
[25] Zhao, J., Yu, Y., and Wang, Q. Dynamical regulation of epileptiform discharges caused by abnormal astrocyte function with optogenetic stimulation. Chaos Soliton Fract 164:112720(2022). https://doi.org/10.1016/j.chaos.2022.112720
[26] Norton, S.J. Can ultrasound be used to stimulate nerve tissue. Biomed.Eng 2, 6.(2003) https://doi.org/10.1186/1475-925X-2-6

[27] Zhang, Y., Zhang, M., Ling, Z., et al. The influence of transcranial magnetoacoustic stimulation parameters on the basal ganglia-thalamus neural network in parkinson's disease. Fronti Neuosci 15:761720(2021). https://doi.org/10.3389/fnins.2021.761720
[28] Yuan, Y., Pang, N., Chen, Y., et al. A phase-locking analysis of neuronal firing rhythms with transcranial magneto-acoustical stimulation based on the Hodgkin-Huxley neuron model. Front Comput Neurosci 11:1(2017). https://doi.org/10.3389/fncom.2017.00001
[29] Zhou, X., Liu, S., Wang, Y., et al. High-resolution transcranial electrical stimulation for living mice based on magneto-acoustic effect. Front Neurosci 13:1342(2019). https://doi.org/10.3389/fnins.2019.01342
[30] McLean, M.J., Engström, S., Zhang, Q., et al. Effects of a static magnetic filed on audiogenic seizures in black Swiss mice. Epilepsy Res 80(2-3):119-131(2008). https://doi.org/10.1016/j.eplepsyres.2008.03.022
[31] Qiu, Z., Kala, S., Guo, J., et al. Targeted neurostimulation in mouse brains with non-invasive ultrasound. Cell Rep 32(7):108033 (2020). https://doi.org/10.1016/j.celrep.2020.108033
[32] Olufsen, M., Whittington, M., Camperi, M. et al. New functions for the gamma rhythm: population tuning and preprocessing for the beta rhythm. J Comput Neurosci 14(1):33-54(2003). https://doi.org/10.1023/A:1021124317706
[33] Hodgkin, A.L. and Huxley, A.F. Currents carried by sodium and potassium ions through the membrane of the giant axon of loligo. J Physiol 116(4):449-472(1952). https://doi.org/10.1113/jphysiol.1952.sp004717
[34] Wang, X. and Buzśaki, G. Gamma oscillation by synaptic inhibition in a hippocampal interneuronal network model. J Neurosci 16(20):6402-6413(1996). https://doi.org/10.1523/JNEUROSCI.16-20-06402.1996
[35] Kopell, N., Börgers, C., Pervouchine, D., et al. Gamma and theta rhythms in biophysical models of hippocampal circuits. In: Cutsuridis V, Graham B, Cobb S, et al. (eds) Hippocampal Microcircuits. Springer series in computational neuroscience, vol 5. p. 423-457. Springer, New York(2010).
[36] Bernhardt, B.C., Chen, Z., He, Y., et al. Graph-theoretical analysis reveals disrupted small-world organization of cortical thickness correlation networks in temporal lobe epilepsy. Cereb Cortex 21: 2147-2157(2011). https://doi.org/10.1093/cercor/bhq291
[37] Montalibet, A., Jossinet, J., Matias, A., and Cathignol, D. Electric current generated by ultrasonically induced Lorentz force in biological media. Med Biol Eng Comput. 39,15–20 (2001).doi:10.1007/BF02345261

[38] Yuan, Y., Chen, Y. and Li, X. Theoretic analysis of transcranial magneto-acoustical stimulation with Hodgkin-huxley neuron model. Front Comput Neurosci 10:35 (2016). https://doi.org/10.3389/fncom.2016.00035
[39] Hendee, W.R. and Ritenour, E.R. Medical Imaging Physics, 4th Edn. John Wiley & Sons, New York (2002).
[40] Treeby, B.E. and Cox, B.T. k-Wave: MATLAB toolbox for the simulation and reconstruction of photoacoustic wave fields. J Biomed Opt 15(2):021314(2010). https://doi.org/10.1117/1.3360308
[41] Tufail, Y., Yoshihiro, A., Pati, S., et al. Ultrasonic neuromodulation by brain stimulation with transcranial ultrasound. Nat Protoc 6:1453–1470(2011). https://doi.org/10.1038/nprot.2011.371
[42] Gnatkovsky, V., Librizzi, L., Trombin, F., et al. Fast activity at seizure onset is mediated by inhibitory circuits in the entorhinal cortex in vitro. Ann Neurol 64: 674–686(2008). https://doi.org/10.1002/ana.21519
[43] Magloire, V., Savtchenko, L.P., Jensen, T.P., et al. Volume-transmitted GABA waves pace epileptiform rhythms in the hippocampal network. Curr Biol 33:1-16(2023). https://doi.org/10.1016/j.cub.2023.02.051
[44] Barrio, R., Ibáñez, S., Pérez, L., et al. Spike-adding structure in fold/hom bursters. Commun Nonlinear Sci Numer Simulat 83:105100(2020). https://doi.org/ 10.1016/j.cnsns.2019.105100
[45] Barreto, E. and Cressman, J.R. Ion concentration dynamics as a mechanism for neuronal bursting. J Biol Phys 37:361-373(2010). https://doi.org/10.1007/s10867-010-9212-6
[46] Florence, G., Pereira, T. and Kurth,s J. Extracellular potassium dynamics in the hyperexcitable state of the neuronal ictal activity. Commun Nonlinear Sci Numer Simulat 17:4700-4706(2012). https://doi.org/ 10.1016/j.cnsns.2011.06.023
[47] Howe, Timothy., Blockeel, A.J., Taylor, H., et al. NMDA receptors promote hippocampal sharp-wave ripples and the associated coactivity of CA1 pyramidal cells. Hippocampus 30:1356-1370(2020). https://doi.org/10.1002/hipo.23276
[48] Wang, Y., Feng, L., Liu, S., et al. Transcranial magneto-acoustic stimulation improves neuroplasticity in hippocampus parkinson's disease model mice. Neurotherapeutics 16(4):1210-1224(2019). https://doi.org/10.1007/s13311-019-00732-5
[49] Liu, R., Ma, R., Liu, X., et al. A noninvasive deep brain stimulation method via temporal-spatial interference magneto-acoustic effects: simulation and experimental validation. IEEE T Ultrason Ferr 69(8):2474-2483 (2022). https://doi.org/10.1109/TUFFC.2022.3187748